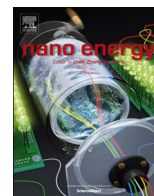




ELSEVIER

Contents lists available at ScienceDirect

Nano Energy

journal homepage: [www.elsevier.com/locate/nanoen](http://www.elsevier.com/locate/nanoen)

# Enhanced electrochemical performance promoted by monolayer graphene and void space in silicon composite anode materials



Xuli Ding<sup>a</sup>, XiaoXiao Liu<sup>b</sup>, Yangyang Huang<sup>b</sup>, Xuefu Zhang<sup>c</sup>, Qianjin Zhao<sup>b</sup>,  
Xinghua Xiang<sup>b</sup>, Guolong Li<sup>b</sup>, Pengfei He<sup>d</sup>, Zhaoyin Wen<sup>e</sup>, Ju Li<sup>a,f,\*</sup>, Yunhui Huang<sup>a,b,\*</sup>

<sup>a</sup> Collaborative Innovation Center of Intelligent New Energy Vehicle, School of Materials Science and Engineering, Tongji University, Shanghai 201804, China

<sup>b</sup> School of Materials Science and Engineering, Huazhong University of Science and Technology, Wuhan, Hubei 430074, China

<sup>c</sup> State Key Laboratory of Functional Materials for Informatics, Shanghai Institute of Microsystem and Information Technology, Chinese Academy of Sciences, Shanghai 200050, China

<sup>d</sup> School of Aerospace Engineering and Applied Mechanics, Shanghai 200092, China

<sup>e</sup> CAS Key Laboratory of Materials for Energy Conversion, Shanghai Institute of Ceramics, Chinese Academy of Sciences, Shanghai 200050, China

<sup>f</sup> Department of Nuclear Science and Engineering and Department of Materials Science and Engineering, Massachusetts Institute of Technology, Cambridge, MA 02139, United States

## ARTICLE INFO

### Article history:

Received 9 May 2016

Received in revised form

24 July 2016

Accepted 25 July 2016

Available online 1 August 2016

### Keywords:

Nano-silicon

Monolayer graphene

Chemical vapor deposition

Melt-self-assembly

Composite anode

## ABSTRACT

The high specific capacity battery electrode materials have stimulated great research interest. Silicon (Si) as a low-cost abundant material with a theoretical specific capacity of  $4200 \text{ mA h g}^{-1}$ , offers an attractive option for the low-cost next-generation high capacity Li-ion batteries anode. However, successful applications of silicon anode have been impeded by several limitations such as large volume expansion (400%) with lithiation, poor conductivity and unstable solid electrolyte interphase (SEI) with cycles. To address these challenges, we engineered Si nanoparticles by encapsulating them with monolayer graphene (mGra) with empty space generated by melt-self-assembly Cu layer. Here, a new method is introduced to uniform encapsulate the nano-silicon particles. The synthesis process used low-cost Si nanoparticles and Cu foils via chemical vapor deposition methods. The mGra and void space around the Si nanoparticles guaranteed to overcome mentioned problems. The flexibility nature and high conductivity of mGra effectively accommodate the Si volume expansion associated with the lithiation, and function as charges fast channels that allow for ions and electrons transport in fast kinetics. Most important, the crystalized mGra layer served as a flexible protective layer avoiding the SNPs direct exposed to electrolyte, which boosted the formation of stable and thin SEI interface. Our anode demonstrated a high initial coulomb efficiency (CE) 85% with gravimetric capacity  $\sim 1450 \text{ mA h g}^{-1}$  (based on the total mass) and long cycle life (500 cycles with 89% capacity retention). Such SNP@void@mGra structure orienting excellent cycle life and high charge capacity provide a promising prospect for the next-generation high specific energy battery.

© 2016 Elsevier Ltd. All rights reserved.

## 1. Introduction

Lithium-ion batteries (LIBs) for consumer electronics, electric vehicles and grid-scale energy storage need to meet the simultaneous challenges of safety, energy density, cycle life and cost [1–3]. Electrode materials are key for electrochemical performance. For the anode materials, silicon (Si) is likely used in ever greater proportion for the next-generation batteries because of its high

energy density, natural abundance, low cost, and environmental friendliness [4–15]. However, large volume expansion, poor electrical conductivity, low initial and steady-state Coulomb Efficiency (CE) and unstable solid-electrolyte interphase (SEI) are the key problems [16–20]. Significant research efforts have been devoted to overcome these issues [19–29]. Among them, nanosized Si shows a potential opportunity due to fast electrode kinetics and excellent thermal and mechanical characters [20–22,24]. However, for the nanostructured Si particles, large surface area still increase side reactions and overload SEI during repeated cycling, which eventually leads to electrical disconnection, poor cycle life and low CE. In this regard, careful design of nano-Si electrode is required to obtain an optimized balance between the surface protection and

\* Corresponding authors at: Collaborative Innovation Center of Intelligent New Energy Vehicle, School of Materials Science and Engineering, Tongji University, Shanghai 201804, China.

E-mail addresses: [liju@mit.edu](mailto:liju@mit.edu) (J. Li), [huangyh@hust.edu.cn](mailto:huangyh@hust.edu.cn) (Y. Huang).

space availability for the perfect battery performance. To develop desirable nano-Si based anodes, the following strategies should be considered: (1) enough nanoscaled void space created to accommodate the large volume expansion, (2) conductive and flexible matrices provided to improve the conductivity and buffer the volume change, and (3) Si surface protection designed to promote the formation of stable and thin SEI in order to decrease the irreversible capacity loss. For example, hollow core-shell or yolk-shell architectures containing Si core and C shell are effective for high performance [18,24,29]. However, most of the architectures are based on the introduction of conducting amorphous carbon or chemically-derived graphene (Gra) oxide (GO) [28–36]. In general, amorphous carbon or GO often results in brittleness, flaws and poor conductivity, leading to large irreversibility [37,38]. Crystallized monolayer or few-layer graphene (fGra) can offer more flexibility to accommodate the large volume change, and more effective routes for electrons and thermal conduction. Compared with amorphous carbon ( $\sim 20$  GP) or GO [39], mGra shows superior flexibility and structural stability [40], which can accommodate larger volume change and preserve better structure integration for Si electrode.

Recently two research work just reported the Si-Gra composite anodes for LIBs [17,41], the direct anchor graphene onto Si surface can accommodate some volume expansion of silicon, but the bearing strength is limited via the sliding process [17], while the electroless deposition Ni layer can serve as dual effect: catalyst and sacrificial layer for generating void space [41], but using Ni as catalyst, the Gra layer number is difficult to control due to the dissolution and precipitation mechanism for Gra growth [42], which is completely different from the Cu catalyst with surface adsorption function and the monolayer Gra is easy to be controllably synthesized on Cu surface. In this work, we encapsulate Si nanoparticles (SNPs) by monolayer graphene (mGra) with designed void space between SNPs and mGra created by molten Cu template chemical vapor deposition. Such synthesis method shows several advantages: (1) mGra can accommodate large strain and stress, which is different from the previously-reported multilayer Gra, GO and amorphous carbon; (2) the molten Cu route facilitates uniform and fully encapsulated Cu layer outside the nanostructure Si, which is difficult achieved for the other methods such as magnetron sputtering, etc.; (3) the void space is created by nitric acid etching and its size can be easily adjusted; (4) our simple and facile synthesis has potential for mass production. SNPs can dwell in the built-in void space of mGra shell with face-to-face rather than point-by-point contact mode [43], which can greatly extend the Si-C contact interfacial area and then create more efficient channels for fast transport of both electrons and ions. The mGra's flexibility and the void space between each SNP and mGra, accommodate the SNP expansion without rupturing the protective layer, which ensures the formation of a stable and thin SEI layer on the outer surface. Moreover, mGra and the void space work synergistically as following: although the void space was left to accommodate the volume change, yet the void size cannot be too large in order to maintain the volumetric capacity, for example, for a 50 nm silicon nanoparticles, considering the 400% volume expansion, a 15 nm void space should be set aside for accommodating the volume expansion, but due to the anisotropy [44–46] of the expanding silicon, one direction volume expansion may exceed 15 nm for lithiation, while the another direction cannot reach this far, and then the flexible mGra can help to accommodate the volume and shape change.

## 2. Experiment section

### 2.1. Materials synthesis

Synthesis mGra on nano-Si: SNPs used in this work were purchased from Shanghai Haotian Nano Company. A facile melting-self-assembly method was employed to fabricate the SNP/Gra composites. The commercial SNPs were first coated with Cu layer (Cu foil, 99.5%, Alfa Aesar) in an atmospheric CVD furnace at 1100 °C for 1 h under Ar and H<sub>2</sub>. Then, the furnace was quickly cooled down to 950 °C to make the melted Cu self-assembly onto SNP surface. At the same time, graphene was *in situ* grown on to Cu layer by flowing 10 standard cubic centimeters (sccm) of CH<sub>4</sub>, 20 sccm H<sub>2</sub> and 200 sccm Ar under atmospheric pressure at 950 °C for 40 min to form monolayer Gra and for 60 min to form few-layers Gra. Thus SNP@Cu@Gra architecture was achieved. The Cu layer was then sacrificed by diluted nitric acid aqueous solution (1:1 with de-ionized water) to finally form SNP@void@Gra composite.

### 2.2. Materials characterization

The morphologies and elements mapping of SNPs and the SNPs-based composites were observed by field-emission SEM (FEI Nova NanoSEM 45). TEM and HRTEM images were attained on a JEOL JEM-2100 instrument equipped with a CCD camera by operating at an acceleration voltage of 200 kV. Elemental analysis was performed using energy-dispersive X-ray spectroscopy (EDS) attached in TEM. Raman spectroscopy was detected at an operating power level of 2 mW on a confocal Raman spectrometer (ThermoFisher, US) using 532 nm excitation laser with spot size of 0.7  $\mu\text{m}$ . The phase was checked by X-ray diffraction (XRD) on an X'Pert PRO diffractometer (PANalytical B.V., Holland) with high-intensity Cu K<sub>α1</sub> irradiation ( $\lambda = 1.5406 \text{ \AA}$ ). The TG analysis was performed by the vertical zero friction dilatometer L75VS Linseis (Germany) from room temperature to 900 °C in air.

### 2.3. Electrochemical measurements

Electrochemical performances of the composites were investigated on typical coin cells (CR2032) assembled in an Ar-filled glove box. Metal Li foil was used as the counter electrode and Celgard 2300 membrane as the separator. The electrolyte was 1 mol L<sup>-1</sup> LiPF<sub>6</sub> in a mixed solution of ethylene carbonate (EC) and dimethyl carbonate (DMC) (EC: DMC = 1:1). CV curves were measured on a PARSTA 2273 electrochemical workstation at a scanning rate of 0.1 mV s<sup>-1</sup> from 0 to 2 V. Electrochemical impedance spectrum (EIS) measurement was performed within a frequency range between 0.1 Hz and 1 MHz. Galvanostatic charge-discharge tests were carried out on battery measurement system (Land, China) at various current densities within a voltage range of 1.5–0.005 V vs. Li/Li<sup>+</sup> at a constant temperature (25 °C). The electrode was prepared by slurry coating and then dried in oven for 12 h. The ratio of active material: binder (alginate): super P was 8:1:1. The mass loading of the active material on the current collector was  $\sim 0.3$  mg, and the mass loading density per unit area was  $\sim 0.6$  mg cm<sup>-2</sup>. The graphene content in the Si@void@mGra composite was estimated by TGA, which was  $\sim 5$  wt%, as shown in the supporting Fig. S9.

## 3. Results and discussion

Fig. 1(a and b) shows the schematic illustration of the design and synthesis of the SNP@void@mGra composite. SNPs are first wrapped by Cu layer via melt-self-assembly (Fig. 1b), and mGra or

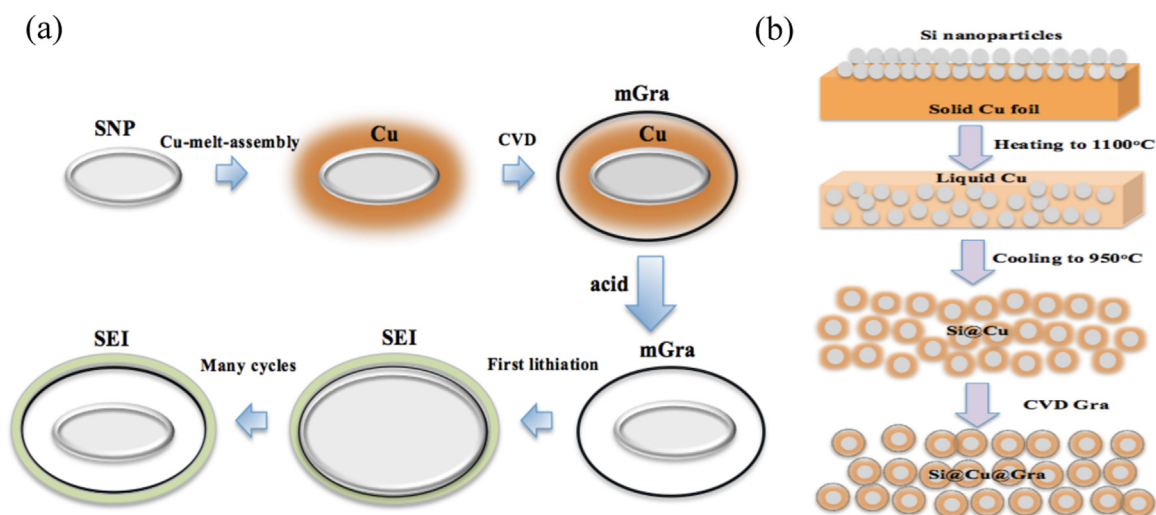


**Fig. 1.** (a) Schematic illustration of melt-self-assembly of Si@void@mGra composite: (I) Cu melt-assembly onto SNP surface; (II) CVD growth of mGra on Cu thin film surface; (III) removal of Cu thin film; (IV) first lithiation in SNP and SEI formation outer the Gra; and (V) after many-cycles lithiation and stable SEI formation. (b) Schematic diagram for formation of Si@Cu and further Si@Cu@Gra composite by melt-self-assembly process.

fGra is *in situ* grown on Cu surface by chemical vapor deposition (CVD). The void is produced by removal of the sacrificial Cu layer using diluted nitric acid. Three kinds of SNP/Gra composites are designed, *i.e.*, SNP@void@mGra, SNP@void@fGra and SNP@dGra. The SNP@dGra is the void-free composite fabricated by direct growth of Gra onto SNP surface without Cu layer via the same CVD process. By tuning the thickness of Cu layer through melting time and temperature, the void space between SNP and mGra layer can be adjusted, which means that the void size in SNP@void@mGra can be well controlled. Since the used SNP have an average diameter around 50 nm, and the volume expansion ratio of Si during lithiation is about 4, the desirable sacrificial Cu layer should have a thickness of  $\sim 15$  nm to allow the expansion of SNP. Based on this, the Cu film thickness in the investigated composites is set to 10–20 nm. More information about the melting self-assembly and Gra growth process is described in Supplementary Fig. S1.

The morphologies of the composites are shown in Fig. 2. From scanning electron microscopy (SEM, Fig. 2a and b) and transmission electron microscopy (TEM, Fig. 2c–i) images, SNPs have particle size around 50 nm. After assembly of Cu film and growth of Gra layer, the particles show some expansion due to incorporation of Cu and Gra (Fig. 2b and c). The elemental mapping in the inset of Fig. 2c clearly indicates the existence of Cu, Si and C. From TEM images in Fig. 2d and e, we can see that SNPs are fully encapsulated uniformly by the *in situ* grown mGra or fGra layer. After removing the Cu intermediate layer of the Si@Cu@Gra, the Si@void@Gra was obtained, and the void space with size in the range of 10–20 nm between SNPs and Gra was clearly visible as indicated in Fig. 2f. The void space is to help accommodate the SNPs volume expansion. It is noteworthy that the built-in void spaces can be controlled by the thickness of Cu sacrificial layer. Fig. 2g, i show high-resolution TEM (HRTEM) images obtained at the edge of the SNP/Gra composites on a grid, confirming *in situ* growth of Gra with monolayer and few layers (mainly 2–5 layers). Here, it should be pointed out that the named mGra or fGra do not refer to the absolute value of the Gra layer number, which is the statistical one according to several measurements and Raman mapping results as indicated by the layer fraction in Fig. 3f. By comparing the morphologies, two kinds of Gra are observed: the mGra or fGra growth on the Si/Cu, and the dGra directly formed on Si surface (Fig. 2i). It is seen that the edges of mGra/fGra are straight and parallel to each other (Fig. 2g and h), indicating high quality and strict stacking orders of the Gra layers; whereas the edges of dGra

are curved stripes (Fig. 2i), corresponding to the disorder and amorphous feature. Furthermore, the selected area electron diffraction (SAED) in the inset of Fig. 2g shows a set of characteristic rings from the polycrystalline SNPs and six-fold symmetric spots from crystallized Gra. Fig. 2j–l give the TEM and HRTEM images of the Si@Cu composite without Gra. It can be seen that the SNPs are fully encapsulated by a layer of Cu shell. After *in-situ* growth of Gra on Cu and then Cu etching by nitric acid, the SNPs/Gra composite is formed. More characterization of the SNPs/Gra composites, including Raman mapping, and X-ray diffraction (XRD) are presented in Fig. 3 and Fig. S3.

Fig. 3a and b show the Raman spectra for the composite. Three characteristic peaks centered at 302, 510, 942  $\text{cm}^{-1}$  are assigned to the nano-silicon particles [47], while the other characteristic peaks around 1350, 1580 and 2700  $\text{cm}^{-1}$  are observed, which are assigned to the D, G and 2D band of Gra, respectively. The mGra growth on Cu layer has higher ratio of  $2D/G > 1$ , which is the typical feature for mGra, while the Gra growth directly on SNP without Cu catalyzer has lower 2D peak height and larger peak width, indicative of more layers and poor crystallization. Since the laser spot size is  $\sim 0.7$   $\mu\text{m}$ , the Raman spectra for nano-Gra ( $< 100$  nm) is somewhat different from the Gra at size  $\sim \mu\text{m}$  or  $\sim \text{cm}$  level. In general, the nano-Gra has higher D peak than G peak due to the enhanced Raman scattering effect. But we can still compare their microstructures by the relative ratio and full width at half maximum (FWHM). It is obvious that the direct growth Gra has wider FWHM, which demonstrates poor crystal and more defects. More information about the microstructural evolution of obtained Gra via various processes can be seen in Fig. S4. Utilizing the Raman spectra mapping, Fig. 3b for the 2D band ( $\sim 2700$   $\text{cm}^{-1}$ ) for a randomly selected  $25 \times 25$   $\mu\text{m}^2$  electrode region (Fig. 3c), as shown in the Raman optical microscopy image for the scanned electrode region, indicate the high uniformity of the synthesized mGra. Raman measurement results for the discretely collected six points within the anode (Fig. 3d) also demonstrate further the uniformity of the synthesized mGra. Fig. 3e shows the Raman spectra for six points collected discretely within the anode, as numbered by (1–6), in Fig. 3d. The results indicate the uniformity of the synthesized mGra. Fig. 3f shows the statistic distribution of layer number for mGra and fGra. It can be seen that the mGra mainly consists of monolayer Gra though other layer number of Gra can be occasionally detected, while the fGra mainly contains Gra with 3–5 layers.

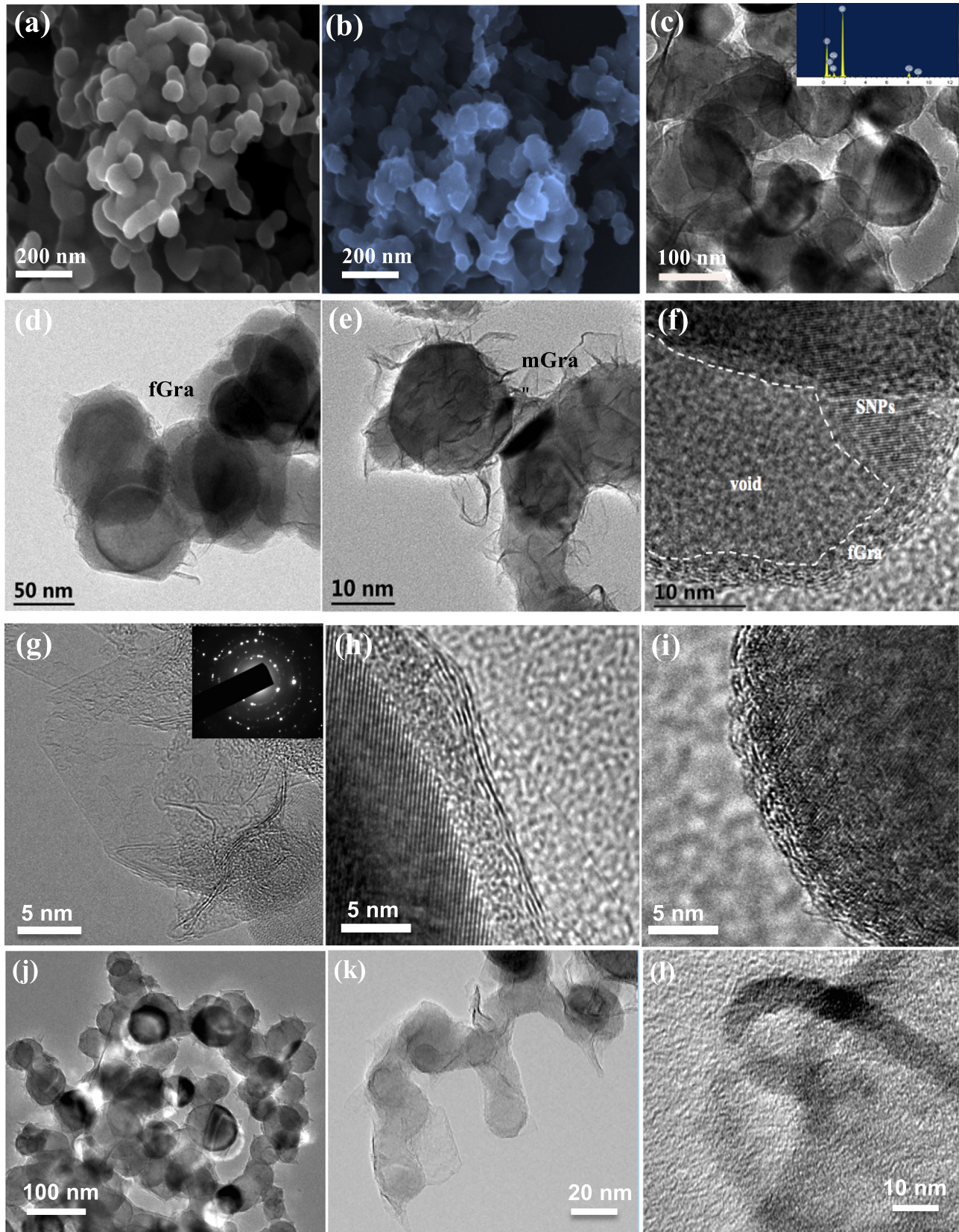


**Fig. 2.** SEM images of (a) bare SNPs and (b) SNPs after melting self-assembly Cu without graphene; TEM images of (c) SNPs encapsulated with Cu layer and Gra (inset shows the elemental analysis), (d) SNP/fGra, and (e) SNP/mGra, (f) Void formation between SNPs and Gra layer, HRTEM images of (g) mGra, (h) fGra and (i) dGra, (j–k) TEM images and (l) HRTEM image of the Si@Cu composite.

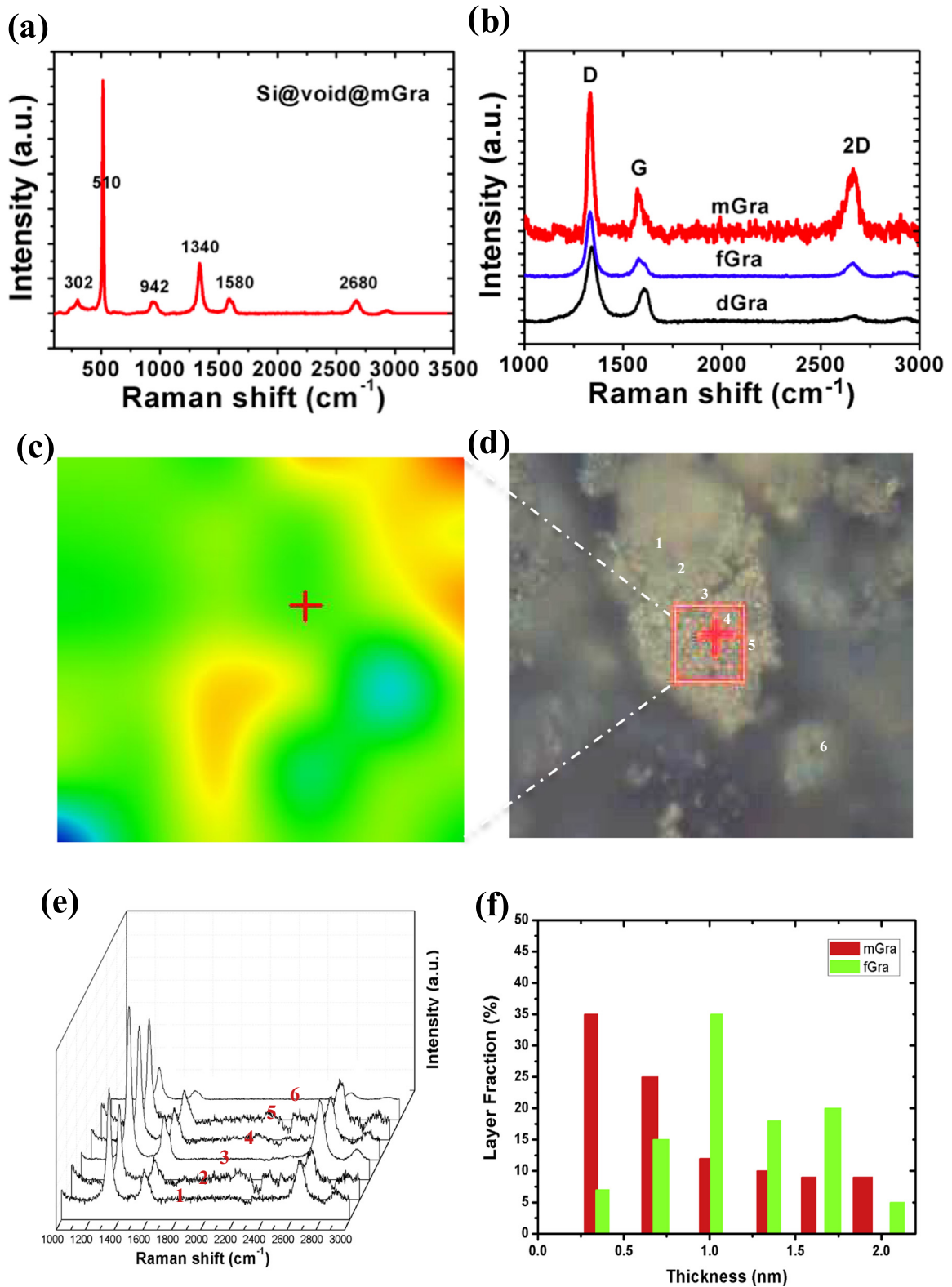


**Fig. 3.** (a) Raman spectra of Si@void@mGra, (b) Raman spectra of mGra, fGra, dGra, (c,d) Raman mapping for the 2D band ( $\sim 2700\text{ cm}^{-1}$ ) for a randomly selected  $25 \times 25\ \mu\text{m}^2$  electrode region. (e) Raman measurement results for the discretionarily collect six points within the anode as labeled in Fig. 3d. (f) The layer number statistics distribute results for mGra and fGra.

In order to further validate the Gra, Cu, Si and void in the composites, corresponding EDS elemental mapping of Si, Cu, and Gra clearly demonstrate that they are homogeneously distributed in the Si@Cu and Si@void@mGra composites as indicated in Fig. 4 and more information about void and void distribution are shown

in the BET analysis in the Supporting Fig. S5.

We evaluated the electrochemical properties of the SNP@void@mGra composites shown in Fig. 1 and compared them with SNP@void@fGra and SNP@dGra. The CV curves of SNP@void@mGra in the initial several cycles are shown in Fig. 5a.

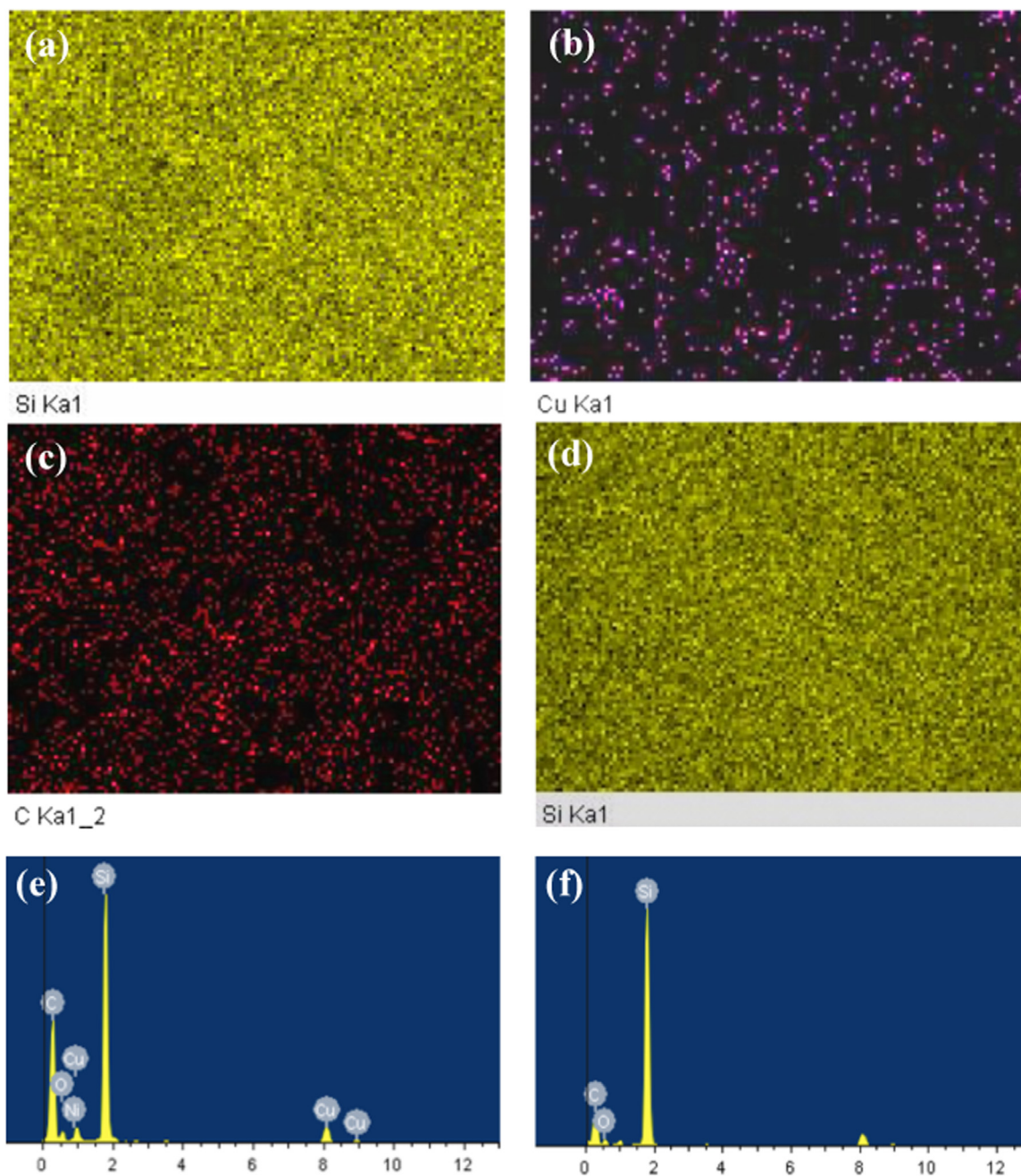
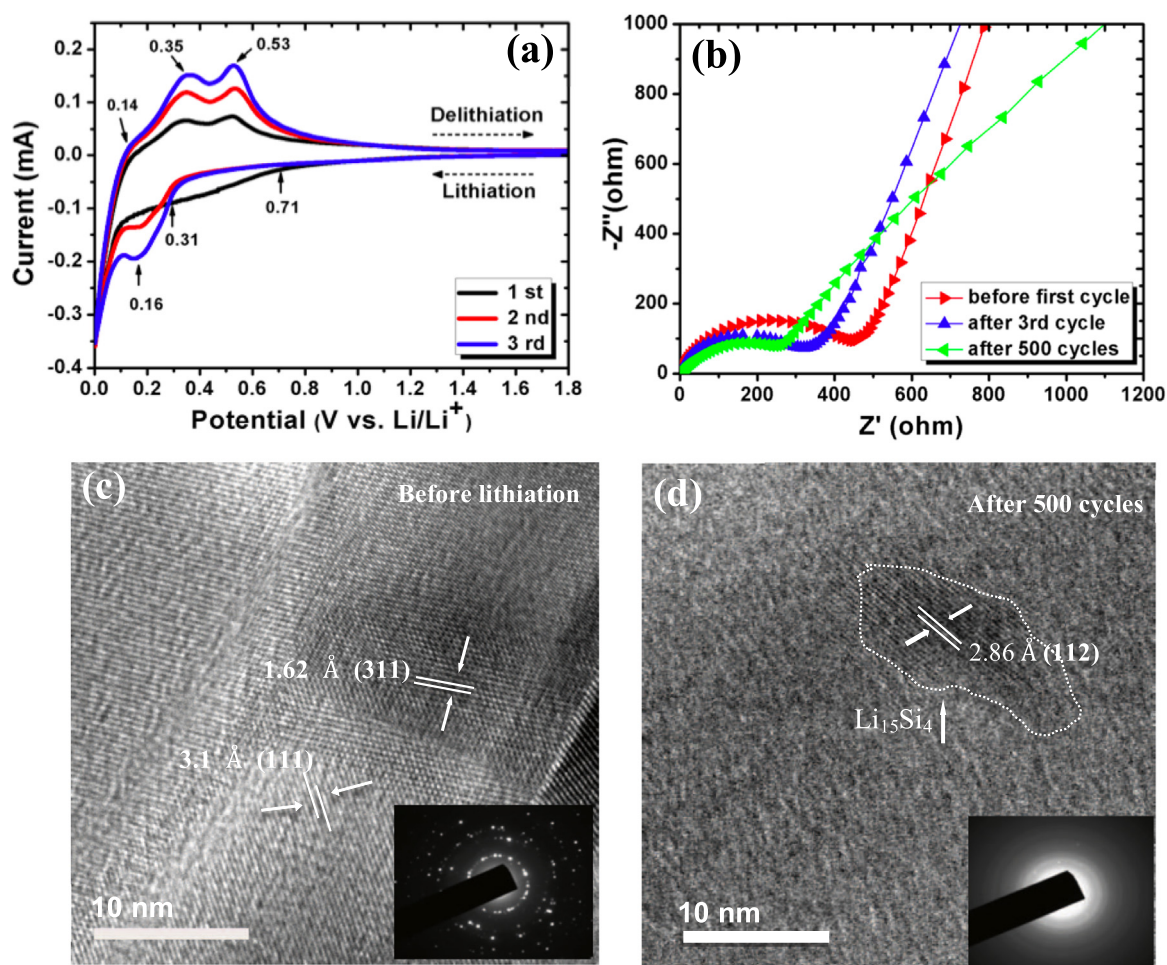


Fig. 4. EDS mapping for the element distribution in Si@Cu and Si@void@Gra.

A broad cathodic peak appears from 0.70 to 0.40 V in the first cycle but disappears in the subsequent cycles. This is mainly due to decomposition of the electrolyte to form SEI film. During the second and third cycle, a new peak appeared at 0.16 V indicates the crystal-to-amorphous transition of SNPs [48–50], which can be further confirmed in Fig. 5c and d. Meanwhile, three broad peaks centered at 0.14, 0.35 and 0.53 V in the following anodic process can be ascribed corresponding to the reverse delithiation. The CV curves demonstrate the reversibility of the constructed electrode, which agree well with the previous reports on the Si-based anodes [25,51–56]. To further check the phase change after cycling, the half-cell was disassembled and the anode was again characterized. Fig. 5c and d show HRTEM images of the SNPs anode before and after 500 cycles. Apparently, its original structure is polycrystalline (Fig. 5c), and the phase of SNPs dominantly becomes amorphous

after 500 cycles, at the same time a small amount of crystal phase of  $\text{Li}_{15}\text{Si}_4$  exists, which agrees well with the results reported [4,10,13]. The SAED in insets of Fig. 5c and d also shows that the diffraction changes from spots to rings, which further demonstrate the transformation from crystal to amorphous phase after cycling. Fig. 5b shows the EIS curves for the SNP@void@mGra electrode before and after running for 3 and 500 cycles to further understand the inner electrochemical impedance and interfacial properties of the SNP-mGra composite. Obviously, the Nyquist plot consists of a suppressed semicircle in high-to-medium frequencies and a diagonal straight line in low frequencies. The former is ascribed to the conduction of ions through the electrolyte, charge transfer, electronic conduction between the active materials and collector, and the external cell connections [18,57–59]; while the latter is attributed to the diffusion of ions from the reaction



**Fig. 5.** (a) A typical CV profile of the SNP@void@mGra electrode at a scanning rate of 0.1 mV/s between 0 and 2 V (*vs.* Li/Li<sup>+</sup>). (b) EIS spectra of the hybrid electrode in the frequency range between 0.1 Hz and 1 MHz. (c-d) HRTEM images for the SNPs before and after 500 cycles, insets are the SAED corresponding.

interface into bulk of the active material and the change of crystal structure [18,57,58,60]. As shown in the EIS curves, a slightly decreased semicircle radius is observed after cycling, which is caused by the activation process of active materials during the repeated cycles and enhanced electronic conduction among the active particles due to the presence of mGra. In the low frequency region, the slope of the slanted straight line slightly increases, indicating the transformation of the polycrystal SNPs into amorphous structure due to the lithiation (Li<sub>x</sub>Si, consistent with the result of HRTEM in Fig. 5d) during the discharge process. In addition, the diffusion resistance of ions may somewhat increases with cycling due to the change of interfacial resistance, but the change is not obvious, which suggests that there is no excess SEI growth at the interface during charging and discharging. This is because the mGra can protect SNPs from being directly exposed to the electrolyte, which can further stabilize the integrity of the Si@void@mGra structure over continuous cycling. The smaller impedance difference upon lithiation and delithiation during the cycling demonstrates the formation of more thin and stable interfacial layer in the SNP@void@mGra electrode. The stable and thin SEI film growth on SNP is very important for the electrochemical performance and cell impedance. Thick and continuous SEI growth can easily result in an impedance increase of the electrode, along with a rapid decrease in capacity over cycling.

Fig. 6a and b show the typical discharge-charge curves of the SNP@void@mGra and SNP@void@fGra composite anodes at the

1st, 10th, 30th, 50th, 70th and 90th cycle under a current density of 500 mA g<sup>-1</sup>. The anode of bare Si without Gra wrap generally has low capacity and poor cyclability due to being oxidized easily without Gra protection and overload SEI formation (Fig. S6). For SNP@void@mGra, during the first cycle, the voltage obviously drops in the range of 0.35–0.70 V, demonstrating the formation of SEI film due to the electrolyte decomposition, which agrees well with the CV curve in Fig. 5a. After then, all the discharge-charge profiles show consistent voltage platform, implying stable electrochemical processes. In the first lithiation process, it delivers an initial discharge capacity of 1450 mA h g<sup>-1</sup> (based on the total mass of SNPs/Gra), while the subsequent delithiation delivers a charge capacity of 1230 mA h g<sup>-1</sup>, giving an initial CE of 85%. The irreversible capacity loss (~15%) in the first cycle is probably associated with the irreversible lithiation and SEI formation. The SEI breakdown and reformation usually result in a poor CE, which is an indicator of the reversibility of the electrode reaction. The initial CE is significantly enhanced as compared with the reported Si-C composite anodes (see Fig. S7), which is mainly attributed to that the mGra formed on the metal Cu catalyzer has high quality and low density of lithium trapping sites as compared with the amorphous or disorder carbon. The CE increases to 97.2% in the second cycle and levels off 99–100% in the subsequent cycles. Therefore, the initial CE, cyclability and rate capability of the SNPs-based anode are remarkably improved by surface modification with Gra, especially mGra. Accordingly, it can be concluded that

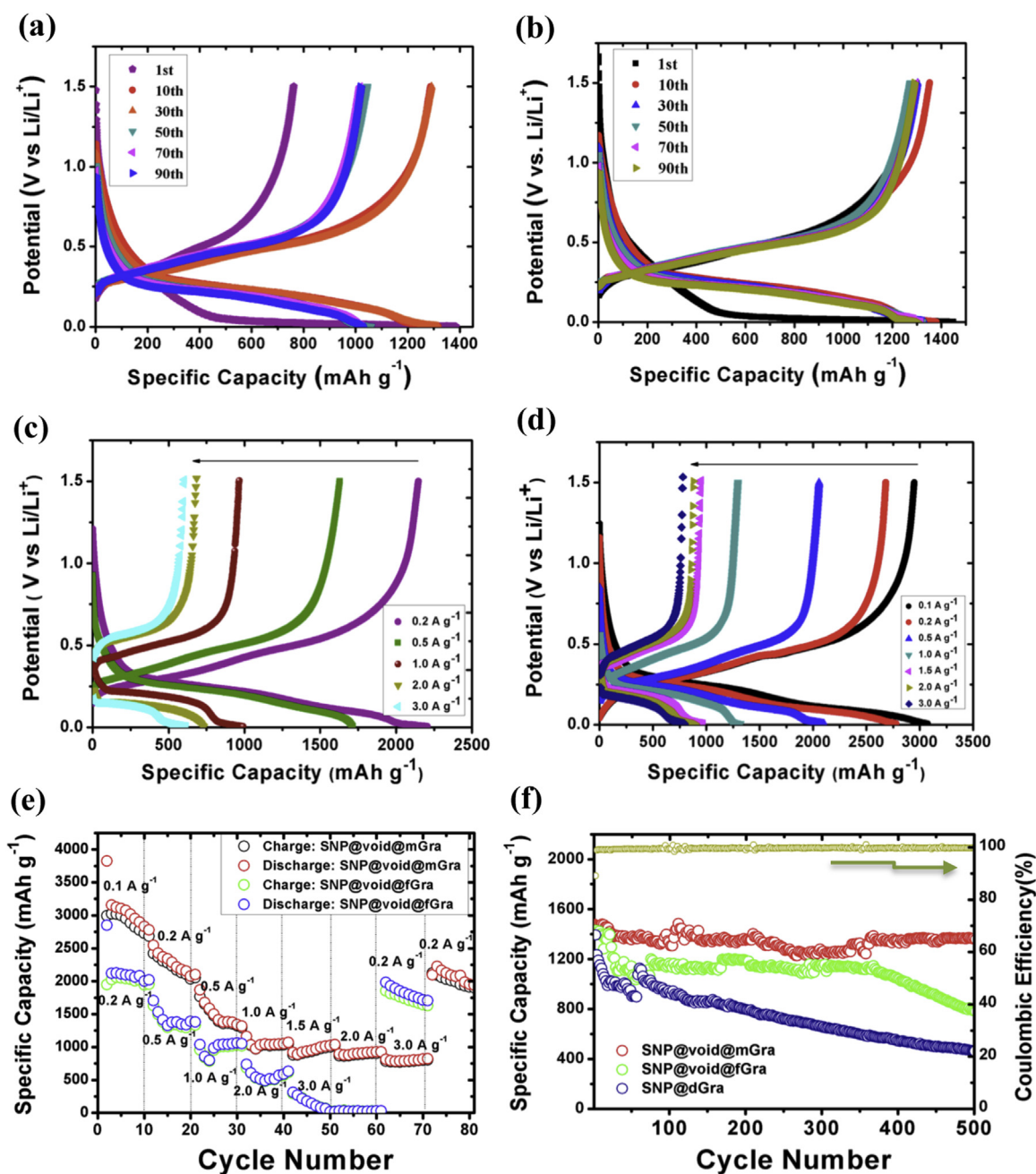


**Fig. 6.** Electrochemical performances of the SNP@void@mGra/fGra anodes. Galvanostatic discharge-charge curves at the 1st, 10th, 30th, 50th, 70th and 90th cycle for (a) SNP@void@fGra, and (b) SNP@void@mGra. Discharge-charge curves at different current densities from 0.1 to 3 A g<sup>-1</sup> for (c) SNP@void@fGra, and (d) SNP@void@mGra. (e) Comparison of charge/discharge capacities at various rates. (f) Comparison of lithiation/delithiation capacity and CE at 0.5 A g<sup>-1</sup> for 500 cycles (SNP@dGra is also compared). All specific capacities are based on the total mass of Gra and SNP.

such surface modification plays a critical role in manipulating stable SEI formation and suppressing side reactions between Si surface and electrolyte.

The discharge-charge performance of SNP@void@mGra was further investigated by cycling at various current densities from 0.1 to 3.0 A g<sup>-1</sup> (Fig. 6c and d). The SNP@void@mGra anode delivers a capacity as high as 3100 mA h g<sup>-1</sup> at 0.1 A g<sup>-1</sup>. The capacity decreases with increasing current density. Even at a high current density of 3.0 A g<sup>-1</sup>, the specific capacity is larger than 800 mA h g<sup>-1</sup>. In addition, in the discharging profiles curves as shown in Fig. 6a–d, a second plateau close to 0 V was identified, which show a steady voltage plateaus for two phase (Li and Li<sub>x</sub>Si) region [61]. A plateau close to 0 V, generally lower than 50 mV vs

Li/Li<sup>+</sup>, indicating a metastable Li<sub>15</sub>Si<sub>4</sub> phase was formed at room temperature, as found in Fig. 5d for the little amount crystal Li<sub>3.75</sub>Si [62,63]. Fig. 6e gives the rate capability for SNP@void@mGra and SNP@void@fGra. The former exhibits capacities of 3100, 2500, 1950, 1200, 1000, 920 and 850 mA h g<sup>-1</sup> at 0.1, 0.2, 0.5, 1.0, 2.0 and 3.0 A g<sup>-1</sup>, respectively; whereas the latter exhibits faster capacity decay. Obviously, the rate capability of SNP@void@mGra is better than that of SNP@void@fGra, especially at high current density due to that mGra has stronger ability than fGra to accommodate high current and provide higher mobility for Li<sup>+</sup> diffusion throughout the whole electrode. The cycling performance at 0.5 A g<sup>-1</sup> are compared in Fig. 6f, here, SNP@dGra is also compared. It is evident that SNP@void@mGra shows the best

cycling stability. For SNP@void@mGra, the capacity only undergoes a short decay during the initial 10 cycles and then becomes nearly stable till 500 cycles. After 500 cycles, a capacity as high as  $1287 \text{ mA h g}^{-1}$  is still maintained, which is 89% retention of the first-cycle capacity. For SNP@void@fGra, the capacity undergoes a rapid decay during the initial 30 cycles, then keeps stable, but decreases again from 350th cycle. After 500 cycles, the capacity drops to  $750 \text{ mA h g}^{-1}$  with retention of only 50%. Though the cyclability of SNP@void@fGra cannot reach SNP@void@mGra, but still better than SNP@dGra. For SNP@dGra, the capacity continuously decreases during 500 cycles, although it delivers a high initial discharge capacity of  $1300 \text{ mA h g}^{-1}$ , only  $350 \text{ mA h g}^{-1}$  is preserved after 500 cycles. Since the three composites have almost the same Gra mass percent, the difference in capacity contributed from the Gra shells can be neglected. Thus, the difference in cycling performance mainly come from the layer number related to the mono-to-few layer Gra (mGra-fGra), the microstructure of different Gra (mGra-dGra), and the void created between SNPs and mGra. Without addition of other special assistance, such as electrolyte additive (for example, FEC), the long cycle life and high capacity of SNP@void@mGra is believed to be originated from the unique designed structure and the nature specialties of the mGra and nano-Si. Firstly, the built-in void space between SNP and mGra allows SNP expand freely without destroying the outer protective layer; Secondly, the mGra layer is conductive for electrons and ions, and face-to-face contact between SNP and mGra can arouse more efficient channels for fast transport of electrons and lithium ions; Finally, the monolayer crystallized mGra can act as an elastic shield to protect Si nanoparticles from directly exposure to the electrolyte, promoting the formation of stable and thin SEI film, which is critical for the long stability of electrode. Whatever, most importantly, the monolayer Gra accompanying with the SNPs encapsulated works as a shielding layer and an electrical highway to provide an excellent elastic buffer backbone for huge expansion of silicon during lithiation, which guarantees a long and stable cycling for the Si-based anodes.

#### 4. Conclusions

In summary, we report nanosized Si-based composites with monolayer graphene fabricated via a new melting self-assembly route with Cu film as sacrificial layer to create void space between Si and graphene. High capacity, long cycle life and excellent rate capability are attained in the SNP@void@mGra composite. The composite exhibits a high initial coulomb efficiency exceeding 85% with discharge capacity of  $3100 \text{ mA h g}^{-1}$  at current density  $0.1 \text{ A g}^{-1}$ . At current  $0.5 \text{ A g}^{-1}$ , 89% capacity retention is achieved over 500 cycles. The monolayer Gra and the void space between Si and Gra not only effectively accommodate the volume change during the lithiation process, but also provide preferential pathways for  $\text{Li}^+$ -ions diffusion. Moreover, good electrical conductivity of mGra facilitates the transport of electrons, and the crystallized Gra serves as a flexible protection layer to avoid Si nanoparticles from being exposed directly to the electrolyte, which is favorable for the formation of stable and thin SEI. It is the synergistic effects of monolayer Gra and void space that effectively solve the large volume expansion with lithiation, poor conductivity, and redundant SEI formation over cycling for the Si-based anodes, and hence achieve superior electrochemical performances. Our present work may provide a potential strategy to develop commercial high-performance Si-based anode materials for next-generation Li-ion batteries.

#### Acknowledgments

The authors gratefully acknowledge the financial support by the National Natural Science Foundation of China (Grant no. 21175050), the PCSIRT (Program for Changjiang Scholars and Innovation Research Team in University, Grant no. IRT14R18), 863 program from the MOST (2015AA034601), and open project (CKEM131408) from the Key Laboratory of energy conversion, Shanghai Institute of Ceramics, CAS. They are also grateful to Mr. Dong Jing, Kongyao Chen and Wang Zhang for valuable discussion.

#### Appendix A. Supporting information

Supplementary data associated with this article can be found in the online version at <http://dx.doi.org/10.1016/j.nanoen.2016.07.031>.

#### References

- [1] B. Dunn, H. Kamath, J.M. Tarascon, *Science* 334 (2011) 928–935.
- [2] M. Armand, J.M. Tarascon, *Nature* 451 (2008) 652–657.
- [3] K. Kang, Y.S. Meng, J. Breger, C.P. Grey, G. Ceder, *Science* 311 (2006) 977–980.
- [4] R.M. Arafat, G. Song, A.I. Bhatt, Y.C. Wong, C. Wen, *Adv. Funct. Mater.* 26 (2016) 647–678.
- [5] M.N. Obrovac, V.L. Chevrier, *Chem. Rev.* 114 (2014) 11444–11502.
- [6] F.M. Hassan, R. Batmaz, J. Li, X. Wang, X. Xiao, A. Yu, Z. Chen, *Nat. Commun.* 6 (8597) (2015) 1–11.
- [7] I.H. Son, J.H. Park, S. Kwon, J.W. Choi, M.H. Rummeli, *Small* 12 (2016) 658–667.
- [8] N. Nitta, F.X. Wu, J.T. Lee, G. Yushin, *Mater. Today* 18 (2015) 252–264.
- [9] N. Nitta, G. Yushin, *Part. Part. Syst. Charact.* 31 (2014) 317–336.
- [10] D.L. Ma, Z.Y. Cao, A.M. Hu, *Nano-Micro Lett.* 6 (2014) 347–358.
- [11] N. Fukata, M. Mitome, Y. Bando, W.Z. Wu, Z.L. Wang, *Nano Energy* 26 (2016) 37–42.
- [12] J.R. Szczech, S. Jin, *Energy Environ. Sci.* 4 (2011) 56–72.
- [13] C.M. Park, J.H. Kim, H. Kim, H.J. Sohn, *Chem. Soc. Rev.* 39 (2010) 3115–3141.
- [14] H. Li, Z.X. Wang, L.Q. Chen, X.J. Huang, *Adv. Mater.* 21 (2009) 4593–4607.
- [15] J. Chen, F.J. Cheng, *Acc. Chem. Res.* 42 (2009) 713–723.
- [16] J.M. Tarascon, M. Armand, *Nature* 414 (2001) 359–367.
- [17] I.H. Son, J.H. Park, S. Kwon, S. Park, H. Mark, A. Bachmatiuk, H.J. Song, J. Ku, J. Wook Choi, J. Choi, S.-G. Doo, H. Chang, *Nat. Commun.* 6 (2015) 7393.
- [18] N. Liu, Z. Lu, J. Zhao, M.T. McDowell, Lee, H.W. Lee, W. Zhao, Y. Cui, *Nat. Nanotechnol.* 9 (2014) 187–192.
- [19] C.K. Chan, H. Peng, G. Liu, K. McIlwrath, X.F. Zhang, R.A. Huggins, Y. Cui, *Nat. Nanotechnol.* 3 (2008) 31–35.
- [20] H. Wu, G. Chan, J.W. Choi, I. Ryu, Y. Yao, McDowell, M.T. McDowell, Lee, S. W. Lee, A. Jackson, Y. Yang, L. Hu, Y. Cui, *Nat. Nanotechnol.* 7 (2012) 310–315.
- [21] M.H. Park, M.G. Kim, J. Joo, K. Kom, J. Kim, S. Ahn, Y. Cui, J. Cho, *Nano Lett.* 9 (2009) 3844–3847.
- [22] I. Kovalenko, B. Zdyrko, A. Magasinski, B. Hertzberg, Z. Milicev, R. Burtovy, I. Luzinov, G. Yushin, *Science* 334 (2011) 75–79.
- [23] Y.H. Xu, Y.J. Zhu, F.D. Han, C. Luo, C.S. Wang, *Adv. Energy Mater.* 5 (2015) 1400753.
- [24] N. Liu, H. Wu, M.T. McDowell, Y. Yao, C.M. Wang, Y. Cui, *Nano Lett.* 12 (2012) 3315–3321.
- [25] A. Magasinski, P. Dixon, B. Hertzberg, A. Kvit, A. Ayala, J.Y. ushin, *Nat. Mater.* 9 (2010) 353–358.
- [26] H. Kim, B. Han, J. Choo, J. Cho, *Angew. Chem. Int. Ed.* 47 (2008) 10151–10154.
- [27] C. Wang, H. Wu, Z. Chen, M.T. McDowell, Y. Cui, Z. Bao, *Nat. Chem.* 5 (2013) 1042–1048.
- [28] S.Q. Chen, P. Bao, X.D. Huang, B. Sun, G.-X. Wang, *Nano Res.* 7 (2014) 85–94.
- [29] S. Chen, M.L. Gordin, R. Yi, G. Howlett, H. Sohn, D.-H. Wang, *Phys. Chem. Chem. Phys.* 14 (2012) 12741–12745.
- [30] M. Ko, S. Chae, S. Jeong, P. Oh, J. Cho, *ACS Nano* 8 (2014) 8591–8599.
- [31] X. Liu, J. Zhang, W. Si, Li Xi, B. Eichler, C. Yan, Q.G. Schmidt, *ACS Nano*, 9, (2015) 1198–1205.
- [32] X. Zhao, C.M. Hayner, M.C. Kung, H. Harold, *Adv. Energy Mater.* 1 (2011) 1079–1084.
- [33] X.S. Zhou, Y.X. Yin, L.J. Wan, Y.G. Guo, *Adv. Energy Mater.* 2 (2012) 1086–1090.
- [34] J.G. Ren, C.D. Wang, Q.H. Wu, X. Liu, Y. Yang, L.F. He, W.J. Zhang, *Nanoscale* 6 (2014) 3353–3360.
- [35] J.B. Chang, X.K. Huang, G.H. Zhou, S.M. Cui, S. Mao, J.H. Chen, *Nano Energy* 15 (2015) 679–687.
- [36] J. Zhang, L. Zhang, P. Xue, L.Y. Zhang, X.L. Zhang, W.W. Hao, J.H. Tian, M. Shen, H.H. Zheng, *J. Mater. Chem. A* 3 (2015) 7810–7821.

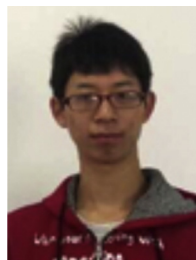
- [37] Z.J. Li, B.C. Yang, S.R. Zhang, C.M. Zhao, Appl. Surf. Sci. 258 (2012) 3726–3731.
- [38] S.R. Mukai, T. Hasegawa, M. Takagi, H. Tamon, Carbon 42 (2004) 837–842.
- [39] X. Jiang, K. Reichelt, B. Stritzker, J. Appl. Phys. 66 (1989) 5805–5808.
- [40] J.-U. Lee, D. Yoon, H. Cheong, Nano Lett. 12 (2012) 4444–4448.
- [41] Y.Z. Li, K. Yan, H.-W. Lee, Z.D. Lu, N. Liu, Y. Cui, Nat. Energy 1 (15029) (2016) 1–8.
- [42] X.S. Li, W.W. Cai, L. Colombo, R.S. Ruoff, Nano Lett. 9 (2009) 4268–4272.
- [43] B. Wang, X.L. Li, X.F. Zhang, B. Luo, Y.B. Zhang, L.J. Zhi, Adv. Mater. 25 (2013) 3560–3565.
- [44] X.H. Liu, H. Zheng, L. Zhong, S. Huang, K. karki, L.Q. Zhang, Y. Liu, A. Kushima, W.T. Liang, J.W. Wang, J.-H. Cho, E. Spstein, S.A. Dayeh, S.T. Picraux, T. Zhu, J. Li, J.P. Sullivan, J. Cumings, C. Wang, S.X. Mao, Z.Z. Ye, S. Zhang, Y. Huang, Nano Lett. 11 (2011) 3312–3318.
- [45] S.W. Lee, M.T. McDowell, J.W. Choi, Y. Cui, Nano Lett. 11 (2011) 3034–3039.
- [46] J.L. Goldman, B.R. Long, A. Gewirth, R.G. Nuzzo, Adv. Funct. Mater. 21 (2011) 2412–2422.
- [47] C. Meier, S. Luttjohann, V.G. Kravets, H. Nienhaus, A. Lorke, H. Wiggers, Physica E 32 (2006) 155–158.
- [48] F. Wang, S. Xu, S. Zhu, H. Peng, R. Huang, L. Wang, X. Xie, P.K. Chu, Electrochim. Acta 87 (2013) 250–255.
- [49] C.K. Chan, H. Peng, G. Liu, K. McClwrath, X.F. Zhang, R.A. Huggins, Y. Cui, Nat. Nanotechnol. 3 (2008) 31–35.
- [50] H. Kim, J. Cho, Nano Lett. 8 (2008) 3688–3691.
- [51] A. Magasinski, P. Dixon, B. Hertzberg, A. Kvit, J. Ayala, G. Yushin, Nat. Mater. 9 (2010) 353–358.
- [52] M.Y. Ge, J.P. Rong, X. Fang, C.W. Zhou, Nano Lett. 12 (2012) 2318–2323.
- [53] W.Y. Li, Y.B. Tang, W.P. Kang, Z.Y. Zhang, X. Yang, Y. Zhu, W.J. Zhang, C.S. Lee, Small 11 (2015) 1345–1351.
- [54] X.S. Zhou, Y.X. Yin, L.J. Wan, Y.G. Guo, Chem. Commun. 48 (2012) 2198–2200.
- [55] X.H. Yu, F.H. Xue, H. Huang, C.J. Liu, J.Y. Yu, Y.Y. Sun, X.L. Dong, G.Z. Cao, Y. G. Jung, Nanoscale 6 (2014) 6860–6865.
- [56] P. Wu, Wang, H. Wang, Y.W. Tang, Y.M. Zhou, T.H. Lu, ACS Appl. Mater. Interfaces 6 (2014) 3546–3552.
- [57] J.B. Chang, X.K. Huang, G.H. Zhou, S.M. Cui, P.B. Hallac, J.W. Jiang, P.T. Hurley, J. H. Chen, Adv. Mater. 26 (2014) 758–764.
- [58] R. Ruffo, S.S. Hong, C.K. Chan, R.A. Huggins, Y. Cui, J. Phys. Chem. C 113 (2009) 11390–11398.
- [59] R. Delevie, Electrochim. Acta 9 (1964) 1231–1245.
- [60] E. Barsoukov, J.R. Macdonald, 2nd (ed.), John Wiley Sons. Inc. Hoboken, NJ, 2005.
- [61] C.J. Wen, R.A. Huggins, J. Solid State Chem. 37 (1981) 271–278.
- [62] J. Li, J. Dahn, J. Electrochem. Soc. 154 (2007) A156–A161.
- [63] M. Obrovac, L. Christensen, Electrochem. Solid-State Lett. 7 (2004) A93–A96.



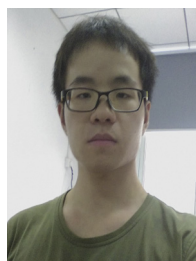
**Yangyang Huang** received his B.S. degree from East China Institute of Technology in 2014. He is now a master student in Wuhan Institute of Technology and a visiting student in Huazhong University of Science and Technology. He focuses on electrode materials for sodium-ion batteries.



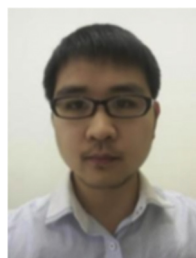
**Xuefu Zhang** received his B.S. from Linyi University in 2009, received his M.S. in Nanchang University in 2012. Currently, he is a Ph.D. candidate in Shanghai Institute of Microsystem and Information Technology, Chinese Academy of Sciences. He mainly works on fabrication of single-crystalline graphene, controllable direct graphene growth on dielectric substrates by chemical vapor deposition method and the application of graphene.



**Qianjin Zhao** is presently a master degree candidate at Professor Huang's group in Huazhong University of Science and Technology. He received his bachelor in Central South University in 2014.



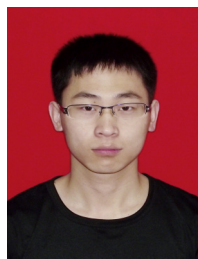
**Xinghua Xiang** is currently a master student at Professor Huang's group in Huazhong University of Science and Technology. His research interest mainly focuses on electrode materials for sodium-ion batteries.



**Guolong Li** is a Ph.D. candidate in Huazhong University of Science and Technology, China. He works on electrode materials for electrochemical energy storage.



**Xuli Ding** received her Ph.D. from Shanghai Jiao Tong University in 2012. During 2012–2014, she worked as a postdoctoral researcher at Seoul National University. She is now a Researcher Associate in Tongji University, Shanghai. Her research interest is focused on new nanomaterials and their application in energy storage and conversion.



**Xiaoxiao Liu** is a Ph.D. candidate in School of Materials Science and Engineering, Huazhong University of Science and Technology, China. He is working on nanostructured materials for electrochemical energy storage.



**Pengfei He** received his Ph.D. degree from Xian Jiao-Tong University in 1992. In 1993 he joined Tongji University as an associate Professor. He worked as a postdoctor in Cambridge University from 1997 to 1998, and as a senior visiting scholar in HongKong University in 2002, in Max Planck Institute in 2003. From 2003 to now, he is a Professor in Tongji University.



**Ju Li** received his Ph.D. from Massachusetts Institute of Technology (MIT) in 2000. From 2000 to 2002, he worked as postdoctoral associate in MIT. From 2002 to 2007, he worked as Assistant Professor In Ohio State University. From 2007 to 2011, he worked as an Associate Professor in University of Pennsylvania. From 2011 to present, he is a full Professor in MIT.



**Zhaoyin Wen** received his Ph.D. from Shanghai Institute of Ceramics, Chinese Academy of Sciences in 1998. From 1999 to 2011, he worked as a visiting professor in Mie University, Japan. Since 1999, he has been employed as a full professor in Shanghai Institute of Ceramics and worked on secondary batteries and energy storage technologies.



**Yunhui Huang** received his Ph.D. from Peking University in 2000. From 2002 to 2004, he worked as an associate professor in Fudan University and a JSPS fellow in Tokyo Institute of Technology (Japan). From 2004 to 2007, he worked with Professor John Goodenough in the University of Texas at Austin. In 2008, he became a chair professor of materials science in Huazhong University of Science and Technology. He is now the dean of the School of Materials Science and Engineering. His research group works on rechargeable batteries for energy storage and their electrode materials. For details please see the lab website: <http://www.sysdoing.com.cn>.